

1 **Assimilation of snow water equivalent from AMSR2 and IMS**
2 **satellite data utilizing the local ensemble transform Kalman filter**

3
4 Joonlee lee¹, Myong-In Lee^{1*}, Sunlae Tak¹, Eunkyo Seo^{2,3}, and Yong-Keun Lee⁴

5
6 ¹ *Department of Civil, Urban, Earth, and Environmental Engineering, Ulsan National*
7 *Institute of Science and Technology, Ulsan, Korea*

8 ² *Department of Environmental Atmospheric Sciences, Pukyong National University, Busan,*
9 *South Korea.*

10 ³*Center for Ocean-Land-Atmosphere Studies, George Mason University, Fairfax, VA, USA*

11 ⁴ *Earth System Science Interdisciplinary Center, University of Maryland, College Park,*
12 *U.S.A.*

13
14
15
16 NOV 15, 2023

17
18
19
20 To be submitted to GMD

21 _____
22 *Corresponding author: Prof. Myong-In Lee, Department of Urban and Environmental

- 23 Engineering, Ulsan National Institute of Science and Technology, 50 UNIST-gil, Ulsan 44919,
- 24 Republic of Korea (milee@unist.ac.kr)

25 **Abstract**

26 Snow Water Equivalent (SWE), as one of the land initial conditions, plays a crucial role in
27 global or regional energy and water balance, thereby exerting a considerable impact on
28 seasonal and sub-seasonal scale predictions owing to its enduring memory over 1 to 2 months.
29 Despite its importance, most SWE initialization remains challenging due to its reliance on
30 simple approaches based on spatially constrained observation. Therefore, this study developed
31 the advanced SWE data assimilation framework with satellite remote-sensing data utilizing the
32 local ensemble transform Kalman filter (LETKF) and the Joint U.K. Land Environment
33 Simulator (JULES) land model. This constitutes a novel approach that has not been previously
34 attempted, as it offers an objective way to optimally combine two imperfect data sources: the
35 satellite SWE retrieval from the Advanced Microwave Scanning Radiometer 2 (AMSR2) and
36 dynamically balanced SWE from JULES land model. In this framework, an algorithm is
37 additionally considered to determine the assimilation process based on the presence or absence
38 of snow cover from the Interactive Multisensor Snow and Ice Mapping System (IMS) satellite,
39 renowned for its superior reliability.

40 The baseline model simulation from JULES without satellite data assimilation shows
41 superior performance in high-latitude regions with heavy snow accumulation but relatively
42 inferior in the transition regions with less snow and high spatial and temporal variation.
43 Contrastingly, the AMSR2 satellite data exhibit better performance in the transition regions but
44 poorer in the high latitudes, presumably due to the limitation of the satellite data in the
45 penetrating depth. The data assimilation (DA) demonstrates the positive impacts by reducing
46 uncertainty in the JULES model simulations in most areas, particularly in the mid-latitude
47 transition regions. In the transition regions, the model background errors from the ensemble
48 runs are significantly larger than the observation errors, emphasizing great uncertainty in the
49 model simulations. The results of this study highlight the beneficial impact of data assimilation

50 by effectively combining both land surface model and satellite-derived data according to their
51 relative uncertainty, thereby controlling not only transitional regions but also satellite-
52 constrained areas experiencing heavy snow accumulation. This assimilation framework is
53 anticipated to contribute to a more precise prediction of atmospheric conditions by realistically
54 capturing the interaction between the atmosphere and land, given the substantial influence of
55 SWE on energy and water balance at the interface of the atmosphere and land.

56

57 **1. Introduction**

58 Snow plays a crucial role in regulating the water, energy, and carbon exchange between the
59 land surface and atmosphere (e.g., Dutra et al., 2011; Thomas et al., 2016). A snowpack tends
60 to increase surface albedo and soil moisture as the snow melts (Eagleson,1970), thereby
61 affecting the climate system through changes in water and energy balances. In addition to local
62 impacts, the continental snowpack over Eurasia can influence the large scale atmospheric
63 circulation during winter (e.g., Li and Wang, 2014) or in spring (e.g., Broxton et al., 2017).
64 Especially, the Eurasian autumn snow can affect upward-propagating stationary Rossby-wave
65 activity, leading to stratospheric warming and weakening of stratospheric polar vortex and jet
66 stream, which in turn emerges as a negative Arctic oscillation (AO)-like pattern at the surface
67 during winter due to downward propagation through the troposphere. Its impact is shown in
68 both observation and model experiments (e.g., Allen and Zender 2011; Cohen et al. 2007).
69 Furthermore, the interannual variability of snow melting during the boreal spring season affects
70 surface soil moisture in summer, which has important implications for heatwave development
71 and emphasizing mechanisms through land-atmosphere interactions (Seo et al., 2020).

72 In the subseasonal to seasonal (S2S) timescales, land initial states are crucial components
73 in the S2S timescale predictions due to the inherent memory that changes slowly for 1 to 2
74 months in the climate system (e.g., Derome et al. 2005; Chen et al., 2010; Seo et al., 2019). In
75 particular, the realistic snow initial states contribute to improving S2S prediction skills, as
76 proven in several modeling studies. For example, previous studies (Orsolini et al., 2013; Jeong
77 et al., 2013) demonstrated a considerable enhancement in prediction skill of 2m air temperature
78 up to a lead time of 1-2 months across certain regions of Eurasia and the Arctic during winter,
79 depending on snow initialization. Moreover, other studies (Orsolini et al., 2016; Li et al., 2019)
80 have revealed that wave activity propagating toward the stratosphere, influenced by snow
81 initial conditions in climate models, can induce changes in the polar vortex and contribute to

82 the persistence of the North Atlantic Oscillation (NAO) and the AO. This emphasizes the
83 significance of snow initialization in climate models as an essential process for enhancing
84 prediction performance at the S2S timescales.

85 Snow states, i.e., snow water equivalent (SWE) used directly for hydrological analysis and
86 initial states of the model (Li et al., 2019; Gan et al., 2021), are generally provided from in-situ
87 observations data, remote-sensing retrievals from satellites, or numerical models such as the
88 land surface model (LSM) operated based on the observed atmospheric variables. For the in-
89 situ data snow depth (SD) measurements prevail, largely attributed to the challenges associated
90 with acquiring precise SWE data (Takala et al., 2011; De Rosnay et al., 2014). Surface synoptic
91 observations (SYNOP) serve as the principal source for SD measurements. The in-situ
92 measurements offer the most dependable snow information, yet they are characterized by
93 relatively coarse temporal and spatial resolutions, particularly within limited areas, due to the
94 spatial heterogeneity inherent in snow distribution. (Helmert et al., 2018; Meyal et al., 2020).
95 Satellite-derived observations using conical scanning microwave instruments may provide
96 spatially consistent data coverage across the globe. Cho et al. (2017) showed the SWE retrieval
97 results from two passive microwave sensors, the advanced microwave scanning radiometer 2
98 (AMSR2) and the special sensor microwave imager sounder (SSMIS). However, the
99 algorithms for SWE retrieval exhibit a degree of sensitivity to a variety of parameters such as
100 snow liquid water content and snow grain size distribution (De Rosnay et al., 2014). Hence,
101 satellite-based SWE data still have limitations in accuracy, especially under deep snow
102 conditions due to the limited penetration depth (Gan et al., 2021). On the other hand, satellite
103 retrieval can estimate snow cover accurately under clear sky conditions (Brubaker et al., 2009).
104 Model simulations obtained from LSMs and simple snow models can cover complete
105 spatiotemporal resolution but involve potentially large uncertainties due to the deficiencies in
106 the physical parameterizations and meteorological forcing data (Dirmeyer et al., 2006; Seo et

107 al., 2021).

108 Considering that snow observation datasets have their respective strengths as well as
109 limitations, data assimilation or other data fusion methods can prove to be beneficial for
110 constructing snow states such as reanalysis data (e.g., Brasnett, 1999; Dee et al., 2011; Meng
111 et al., 2012; Pullen et al., 2011; De Rosnay et al., 2014). For example, the snow analysis for
112 the Canadian Meteorological Center (CMC) utilizes a 2-dimensional optimal interpolation
113 (2D-OI) scheme with in-situ observations and the outputs from a simple snow model (Brown
114 et al., 2003). The National Centers for Environmental Prediction (NCEP) climate forecast
115 system reanalysis (CFSR) combines a multi-satellite-based interactive multi-sensor snow and
116 ice mapping system (IMS) as satellite-based snow cover retrieval and the outputs from the
117 global snow model of the Air Force Weather Agency (Meng et al., 2012). At the European
118 Center for Medium Weather Forecast (ECMWF), the ECMWF reanalysis (ERA)-Interim and
119 ERA5 for the snow analysis employ a Cressman interpolation and 2D-OI, respectively, with
120 the IMS, in-situ observation, and the results from a land surface model (Dee et al. 2011; De
121 Rosnay et al., 2014). The Japanese 55-year Reanalysis (JRA55) also utilizes the 2D-OI with
122 in-situ observation, satellite-based snow cover from SSMIS, and the results from an LSM
123 (Kobayashi et al., 2015). Given that the majority of the reanalysis datasets rely on snow depth
124 measurements, the SWE estimation is likely to introduce potential accuracy concerns when the
125 snow depth information is combined with the snow density calculations.

126 Climate prediction systems in operational centers such as the Meteorological Office (Met
127 Office) in the United Kingdom and the Korean Meteorological Administration (KMA) conduct
128 the snow initialization by utilizing the results of the operational global unified model (UM) and
129 the IMS snow cover, which solely indicates the presence of snow (Pullen et al., 2011), lacking
130 in its ability to reflect the physical quantity of it. The initialization at NCEP also performs a
131 similar approach using input data combined from IMS snow cover and results from the global

132 SD model (SNODEP; Meng et al., 2012). Furthermore, the snow initialization of ECMWF
133 employs optimal interpolation with a combination of results from the LSM, IMS snow cover,
134 and in-situ observation from SYNOP and national networks available on the GTS. However,
135 in regions where ground observations are unavailable, large errors may exist in the snow model
136 outputs due to uncertainties in atmospheric forcing and imperfect model parameterization
137 (Boone et al., 2004; Essery et al., 2009). Often, the snow processes parameterized in LSMs
138 rely on observed properties sampled in limited areas (Lim et al., 2022). In addition, as IMS
139 snow cover only identifies the presence of snow, the data assimilation with the satellite snow
140 cover only is not sufficient and inappropriate in constraining water and energy conservation.
141 Alternative methods that consider the physical quantity of snow are required for the snow
142 initialization.

143 One approach to mitigate the spatial discontinuity of ground observations is to use satellite-
144 derived SWE with wide spatial coverage and frequent temporal resolution. However, the SWE
145 retrievals from satellites still have considerable uncertainties (De Lannoy et al., 2010; Dawson
146 et al., 2018), which can arise from vegetation and terrain interference, sensor signal saturation,
147 snowfall amount, and simplifications in the underlying assumptions of the retrieval algorithms
148 (Liu et al., 2015). In particular, a region with heavy snow accumulation leads to a significant
149 underestimation of SWE due to the limitations in penetration depth from satellites (Gan et al.,
150 2021), so that satellite-derived SWE is not employed in the land initialization process. In
151 previous studies, various approaches have been attempted to improve SWE product
152 performance, such as combining satellite-derived SWE with ground observations (Pulliainen
153 et al., 2020), different satellite data sets (Gan et al., 2021), simple snow models (Dziubanski
154 and Franz, 2016), or LSMs (Kwon et al., 2017; Kumar et al., 2019). However, most previous
155 studies have focused on targeted regions with limited ground-based observations. Snow
156 initialization in global coverage using satellite-derived SWE remains a persistently challenging

157 task.

158 Therefore, this study developed an advanced SWE data assimilation framework with satellite
159 remote-sensing data using the local ensemble transform Kalman filter (LETKF) and the Joint
160 U.K. Land Environment Simulator (JULES) land model. This constitutes a novel approach that
161 has not been previously attempted, and it offers an objective way to optimally combine two
162 imperfect data sources: the satellite SWE from the Advanced Microwave Scanning Radiometer
163 2 (AMSR2) and the dynamically-balanced SWE from the JULES land model forced by
164 observed atmospheric fields. The estimated SWE data exhibit better consistence by
165 additionally using snow cover data from the IMS data. This assimilation framework also
166 enables the assessment of improvement as it provides insights into the reasons behind the
167 performance improvement based on the Kalman gain analysis that measures the relative
168 significance of the input data between the satellite and the land model during the data
169 assimilation cycle. The satellite data have demonstrated high reliability in the transition regions
170 of climatologically-shallow snow conditions (Gan et al., 2021), and these regions are known
171 as "hot spots" of strong atmosphere-land coupling through snow melting and associated surface
172 energy and water balance changes (Koster et al., 2004; Dirmeyer, 2011; Huning and
173 AghaKouchak, 2020). From these perspectives, it would be important to evaluate the impact
174 of satellites on the transition regions as well as on the deep accumulation regions where
175 accurate satellite retrievals are challenging. Furthermore, the benefits of assimilating satellite
176 retrievals in extremely high-temperature events, such as the case in April 2020 over Eurasia,
177 can be elucidated. In this regard, we expect that this snow data assimilation framework with
178 satellite-derived SWE can be significant in providing optimal snow initial states for improving
179 the S2S prediction by global climate models.

180

181 **2. Data and model**

182 **2.1. Satellite data**

183 The snow information including snow cover and SWE can be derived from satellite
184 measurements offering global coverage and high temporal as well as spatial resolution. For
185 data assimilation, this study uses SWE calculated from brightness temperature measurements
186 obtained by the AMSR2 on board the Japanese Aerospace Exploration Agency (JAXA) global
187 change observation mission-water (GCOM-W) satellite. This AMSR2 Unified Level-3 (L3)
188 dataset offers daily estimation of SWE at 25 km resolutions from July 2012 to the present.
189 AMSR2 has a sensor designed to detect microwave radiation naturally emitted from the surface
190 and atmosphere, employing six frequency bands ranging from 6.9 to 89 GHz. Through this
191 conical scanning mechanism, AMSR2 can acquire day and night datasets with nearly constant
192 spatial resolution over more than 99% of the global coverage every two days. Comprehensive
193 explanations of AMSR2 characteristics are available in Imaoka et al. (2010). AMSR2 is
194 selected for the assimilation because it produces more accurate results by assimilating data
195 from modern sensors (e.g., AMSR2) compared to data from conventional sensors (e.g., AMSR-
196 E) (Cho et al., 2017).

197 The widely used multisensor-derived snow cover is IMS (e.g., Ramsay 1998; Helfrich et
198 al., 2007) produced by NOAA the National Environmental Satellite Data and Information
199 Service (NESDIS) for the Northern Hemisphere from February 2004 to the present at 4 km
200 resolutions. This dataset is generated using various data products, including multi-satellite
201 images and in-situ observations (U.S. National Ice Center, 2008). Since IMS provides binary
202 (0: no snow or 1: snow covered) snow cover information, we transform the IMS snow cover at
203 4 km grids to the snow cover fraction (SCF) within a 50-km LSM grid by counting the snow
204 pixel number with a value of 1. A 50-km LSM grid is declared as snow-covered when more
205 than 50% of the 4km pixels within the grid are covered with snow. In this study, the application

206 of the assimilation process is determined based on IMS-based SCF, renowned for its superior
207 reliability (e.g., Brown et al., 2014). Further details will be described in Section 3.3.

208

209 **2.2. Reference data for SWE and SCF**

210 The CMC daily estimated SWE is used for verification. The SWE data is processed using
211 statistical interpolation between a background field derived from a simple snow model and in-
212 situ daily SD (Brown and Brasnett, 2010). In detail, this dataset utilizes optimal interpolation
213 methods to acquire spatial SD from the in-situ data, involving SYNOP, special aviation reports
214 from the World Meteorological Organization (WMO), and meteorological aviation reports
215 (METAR). In areas with scant in-situ data, a simple snow accumulation and melt model is
216 employed to create an optimal interpolation that estimates snowmelt and snowfall worldwide,
217 assuming the persistence of the snowpack mass between snowfall and melting events
218 (Brasnett, 1999). Although the average elevation of snow measurement stations used in CMC
219 is biased toward low elevations ($< 400\text{m}$), potentially causing relative negative biases at higher
220 elevations with heavy snow accumulation, the CMC dataset is often considered the premier
221 snow analysis accessible in the Northern Hemisphere (Su et al. 2010) and has still been widely
222 used to evaluate model outputs (e.g., Reichle et al., 2011; Reichle et al., 2017; Toure et al,
223 2018). Therefore, the SWE of CMC produced without the satellite-derived data is selected for
224 verification as an independent dataset for evaluating the assimilated analysis with remote
225 sensing snow retrievals. Since only daily SD analysis is provided in CMC, it is converted to
226 daily SWE based on the snow bulk density methods (e.g., Sturm et al., 2010). It is available
227 from 12 March 1998 to the present and offers comprehensive coverage of the entire Northern
228 Hemisphere with a horizontal resolution of 24 km. The SWE of CMC at its native horizontal
229 resolution is interpolated onto the LSM grid through local area averaging.

230

231 **2.3. JULES LSM**

232 This study utilizes the JULES LSM from the Met Office (Best et al., 2011), a component
233 land model of the global seasonal forecasting system version 6 (GloSea6) global, fully-coupled
234 atmosphere, ocean, land, and sea-ice model. The surface types (or snow tiles) in the JULES
235 LSM consist of four non-vegetated types: urban, land-ice, inland water, and bare soil, as well
236 as five vegetation functional types: C3 temperate grass, needleleaf trees, shrubs, C4 tropical
237 grass, and broadleaf trees. For each surface tile, a separate energy balance is computed, and the
238 average energy balance in the grid cells is determined by applying weights to the values of each
239 surface tile. Two schemes are used within JULES to represent surface snow (e.g., Best et al.,
240 2011; Burke et al., 2013). The simple method involves a zero-layer approach, which modifies
241 the top soil level without using explicit model layers to represent snow processes. The other is
242 the multi-layer approach which is more comprehensive, described in Best et al. (2011). In the
243 case of vegetated surfaces, snow can be separated into ground snow and canopy snow or stored
244 in a single effective reservoir. As both the zero-layer and multi-layer snow models provide
245 similar results under various conditions (Best et al., 2011), this study used the zero-layer snow
246 model with constant thermal conductivity and density for snow. Although the heat capacity of
247 snow is ignored, the bulk thermal conductivity in the surface layer is reduced as the thermal
248 conductivity of snow differs from that of the soil and the layer thickness increases. As long as
249 snow persists on the ground, the skin temperature cannot exceed 0°C, yet the heat flux utilized
250 for melting the snow is diagnosed as the residual in the surface energy balance. The melted
251 water is immediately drained from the snow, divided into runoff and soil infiltration, and liquid
252 water is not stored or frozen in the snow. A detailed description of the energy and water cycling
253 in the JULES LSM can be referenced in Best et al. (2011).

254 The prognostic variables (e.g., SWE) in the LSM are determined by meteorological forcing
255 variables such as 2-m air temperature, humidity, 10-m wind speed, precipitation, surface

256 pressure, and radiative fluxes. The 3-hourly, JRA55 reanalysis at 0.56° spatial resolution is
257 employed for the meteorological forcing variables, which is linearly interpolated to a 50 km
258 resolution of the LSM. The model background error needed for data assimilation is estimated
259 by JULES ensemble runs with perturbed initial and boundary conditions. Following the
260 previous studies (Reichle et al., 2008; Seo et al., 2021), meteorological forcing variables are
261 perturbed to account for the uncertainties in these variables, especially precipitation, downward
262 shortwave, and downward longwave. Perturbations are applied using additive adjustments
263 assuming a normal distribution for longwave radiation and multiplicative adjustments
264 following a log-normal distribution for shortwave radiation and precipitation, as guided by
265 previous studies (Seo et al., 2021). Here, the ensemble means of additional and multiplicative
266 perturbations are zero and one, respectively. The relationship between disturbed precipitation
267 and radiative flux ensures the physical consistency among atmospheric forcing variables
268 (Reichle et al., 2008). For instance, a negative anomaly in precipitation and downward
269 longwave-radiation is statistically linked to a positive anomaly of downward shortwave-
270 radiation. Detailed explanations regarding the perturbation of atmospheric forcings can be
271 found in Reichle et al. (2008).

272

273 **3. Methodology**

274 **3.1. Bias correction**

275 The discrepancy in SWE between remote sensing and LSMs often arises due to uncertainties
276 in the model physics and forcing data and satellite retrievals. These uncertainties can lead to a
277 significant discrepancy in SWE between model simulations and satellite remote-sensing
278 retrievals, potentially degrading performance. In previous studies (e.g., Reichle and Koster,
279 2004; Seo et al., 2021), a scaling method of the nonlinear cumulative distribution function
280 (CDF) matching is used to account for the systematic bias of soil moisture in the model
281 backgrounds. However, unlike soil moisture, SWE presents varying characteristics in the CDF
282 distribution across different regions, such as between high and low latitudes, thus requiring the
283 estimation of distribution at each grid point. As a result, the insufficient sample size hinders
284 the clear simulation of the CDF distribution, posing challenges in its application. To address
285 this issue, we attempted to apply a simple and effective standard normal deviation scaling to
286 satellite-derived SWE, considering its potential use as initial conditions for JULES LSM-based
287 climate models. Based on the climatology and standard deviation for the model and remote
288 sensing retrievals, the scaled SWE (O_{new}) from the satellite can be derived from the following
289 relation:

290

$$291 \quad O_{new} = \left(\frac{O - \bar{O}}{\sigma_o} \times \sigma_m \right) + \bar{M} \quad (1)$$

292

293 where $\bar{O}(\sigma_o)$ and $\bar{M}(\sigma_m)$ indicate climatology (standard deviation) of remote sensing
294 retrievals and the model, respectively. This approach has been widely utilized in observation-
295 based land initialization and has proven to be effective (e.g., Koster et al., 2011; Jeong et al.,
296 2013).

297

3.2. Data assimilation method

The snow assimilation is conducted based on the LETKF (e.g., Hunt et al., 2007), which is utilized to combine remotely sensed retrievals with the LSM model outputs (a.k.a. backgrounds) to produce a snow analysis. Unlike variational data assimilation methods, non-variational approaches (i.e., ensemble-based filters) characterize a probabilistic representation with the spread of the ensemble serving as an estimate of forecast uncertainty. LETKF has several advantages over other data assimilation methods. First, LETKF can efficiently handle large datasets and high-dimensional state variables by localizing the covariance matrix. This offers efficiency in parallel computing, making it suitable for real-time forecasting and high-resolution data assimilation. In this study, the horizontal local patch size and the localization length scale parameters are defined as 150 km and 30 km (Table 1), respectively. This approach involves the weight function for the covariance localization within the local patch centered at the analysis grid (e.g., Houtekamer and Mitchell, 2001; Hamill et al., 2001). This function assigns larger errors to observations located farther away from the center of the local patch, as proposed by Miyoshi and Yamane (2007), depending on the Gaussian function. Secondly, the method utilizes model simulation ensembles to capture the uncertainty in the initial states and background errors, which allows for a better representation of the flow-dependent probability distribution of the state variables that vary in time and space. Third, the LETKF employs an inflation parameter to adjust the ensemble spread, ensuring realistic uncertainty estimation by accounting for background errors. The underestimation of the analysis error covariance is typically issued by spatially and temporally constant boundary conditions and observation errors and limited ensemble members. Based on the standardized LETKF, this study applies a multiplicative covariance inflation of 20% of the spread of 24 member ensembles for each data assimilation cycle. Furthermore, the Kalman gain analysis (Seo et al., 2021), which quantifies the ratio of the background error to the total error (equivalent to the sum of the background and

323 the observation error), is conducted. This analysis serves to determine the weights assigned to
324 assimilated observations in the analysis update processes of the LETKF.

325

326 **3.3. Snow data assimilation design**

327 This study conducts the advanced snow data assimilation experiment at a daily cycle based
328 on LETKF with the satellite data and the JULES LSM model outputs driven by 3-hourly JRA55
329 reanalysis atmospheric forcing. The snow assimilation processes are illustrated in Fig. 1, with
330 a more detailed description in Table 1. Since data assimilation is conducted by considering the
331 error of SWE in both the model and the observation, it is important to accurately understand
332 the observation and background errors to improve the performance of data assimilation. The
333 experiment calculates the background error from the 24 ensemble member spreads generated
334 by perturbing atmospheric forcings such as longwave radiation, shortwave radiation, and
335 precipitation in JULES LSM, as provided in section 2.3. Due to the absence of precise error
336 estimates for AMSR2 SWE retrievals, the observation error is conservatively prescribed as 10%
337 of AMSR2 SWE for each grid compared to the previous study utilizing AMSR2 SWE data
338 (Lee et al., 2015), considering the general increase in the errors during the snow accumulation
339 period with the development of deep snowpack (Foster et al., 2005; Cho et al., 2017). Here, the
340 bias-corrected AMSR2 satellite data as described in section 3.1 is used as the observation data,
341 and the updated snow analysis state through data assimilation becomes a new initial state for
342 the next integration in JULES LSM (Fig. 1). In addition, the analysis state of this method is
343 calculated based on the IMS snow cover fraction as a reference in the following way (Fig. 1);
344 where the SCF of IMS is zero, the snow amount analysis is set to zero, and in other cases, it is
345 derived from data assimilation. The reason for this is due to the importance of the presence or
346 absence of snow in the climate system, as well as the high reliability of the IMS data (e.g.,
347 Brown et al., 2014). A background experiment of JULES LSM without satellite data

348 assimilation as a baseline (referred to hereafter as “Openloop”) is also achieved by employing
349 the same ensemble perturbations, thereby measuring the skill improvement from the snow
350 analysis state through the assimilation of satellite-derived SWE and IMS SCF from satellite
351 and surface observations (referred to hereafter as “DA”). All experiments are conducted in
352 April from 2013 to 2020, which is one of the months with low snow performance in the LSM
353 when the snow begins to melt in the Northern Hemisphere (e.g., Toure et al., 2018; You et al.,
354 2020).

355 **4. Results**

356 **4.1. Skill Verification**

357 Figure 2 displays the climatological-mean SCF from the IMS multi-satellite data (Brown
358 et al., 2014) and the differences from AMSR2, Openloop, JRA55, and DA for April 2013-2020.
359 Here, the JRA55 SWE serves as a reference dataset for comparison with other reanalyses and
360 is associated with meteorological forcing data used in the JULES land surface model. April is
361 a season when the accumulated snow during the cold season begins to melt. This study defines
362 the transitional region with a climatological-mean SWE of less than 16 mm as in previous
363 studies (e.g., Gan et al., 2021), the boundary of these transition regions is represented by the
364 black lines in Fig. 2. The transitional regions exhibit large variability in space and time, and
365 they are mainly located at mid-latitudes. The SCF climatology patterns show negligible
366 differences in high latitudes of heavy snow accumulation but noticeable differences in the
367 transitional mid-latitude regions of less snow. SCF from JRA55 tends to be underestimated
368 compared to IMS, whereas AMSR2 and Openloop tend to overestimate. There is a clear
369 difference in SCF between AMSR2 and IMS satellite data. This study gives more credibility
370 to IMS than AMSR2, as the former is based on multiple satellite data sources (e.g., Brown et
371 al., 2014). As we used the IMS SCF to define the snow region to be assimilated by AMSR2
372 SWE, it is natural that DA shows better consistency with IMS and reduces overestimation
373 biases in Openloop. Quantitatively, the root mean square differences (accuracy, defined in
374 supplementary Table 1 as in previous study) for AMSR2, Openloop, JRA55, and DA with
375 (from) IMS are 0.23 (0.91), 0.18 (0.91), 0.13 (0.93), and 0.13 (0.97), respectively, showing the
376 best consistency in DA. The quantitative differences between DA and other experimental
377 results are minor, but noticeable spatial discrepancies exist, particularly around transition
378 regions.

379 The SWE climatology from AMSR2, Openloop, JRA55, and DA is also compared with

380 CMC as a reference in Fig. 3. The SWE derived from AMSR2 shows a significant
381 underestimation compared to CMC, particularly in the regions with heavy snow accumulation
382 at high latitudes. This is presumed to be due to limitations in satellite sensors detecting the
383 depth of snow (Gan et al., 2021). The SWE from JRA55 exhibits characteristics of
384 overestimation in high latitudes and underestimation in transitional regions. On the other hand,
385 the climatological SWEs from Openloop and DA exhibit higher correspondence to CMC, even
386 higher than JRA55. Specifically, DA demonstrates a higher agreement with CMC, despite the
387 marginal difference compared to Openloop. Quantitatively, the pattern correlation coefficients
388 (root mean square differences) for AMSR2, Openloop, JRA55, and DA with (from) CMC are
389 0.63 (80.7 kg/m²), 0.80 (50.1 kg/m²), 0.60 (100.8 kg/m²), and 0.80 (49.9 kg/m²), respectively.
390 Due to the application of standard deviation scaling to the satellite-derived SWE used in data
391 assimilation, the discrepancy in climatological SWE distributions between DA and Openloop
392 is deemed negligible. Despite its similarity to Openloop, DA with snow data assimilation
393 displays the relatively highest correlation and the smallest root mean square difference among
394 the datasets.

395 Next, we compare the temporal variation of SWE as measured by the Spearman rank
396 correlation coefficient with CMC, which is regarded as more appropriate than the Pearson
397 correlation coefficient for describing datasets containing nonlinearity and outliers such as snow
398 in both time and space. Figure 4 compares the distribution of correlation skills from AMSR2,
399 Openloop, JRA55, and DA. Openloop has a high performance in regions with heavy snow
400 accumulation but relatively low performance in transition regions with significant snow
401 changes. In contrast, the results from the AMSR2 satellite data represent poor performance in
402 high-latitude areas with heavy snow accumulation but high performance in transitional regions,
403 consistent with the previous studies (Gan et al., 2021). DA shows high performance not only
404 in high-latitude areas with heavy snow accumulation but also in transition regions. Even

405 compared to JRA55 used as the atmospheric forcing, DA performs better in temporal variation.
406 The quantitative results in the correlation in the Northern Hemisphere over 40°N (the transition
407 region) are 0.41 (0.54) for AMSR2, 0.61 (0.48) for Openloop, 0.58 (0.58) for JRA55, and 0.67
408 (0.61) for DA, respectively. The findings indicate that satellite retrievals offer additional value
409 in capturing temporal variations through data assimilation, indicating the benefit of
410 assimilating the AMSR2 SWE despite the overall lower performance of the satellite data itself.

411 The performance improvement by DA is also evident in the zonally-averaged correlation
412 coefficient shown in Fig. 5. The AMSR2 satellite data shows higher performance than
413 Openloop in the transition region around latitude 45 °N-55 °N, although performance sharply
414 decreases with increasing snow accumulation. Openloop indicates gradually increasing
415 performance as the latitude increases, with the highest performance at around 60°N. DA
416 denotes superior performance across the Northern Hemisphere, especially in the mid-latitude
417 transition region than AMSR2 or JRA55. An exception is for 35-40°N in the Tibetan Plateau,
418 where JRA55 used in-situ observations. The results suggest that the developed snow data
419 assimilation system represents well not only the transitional regions but also the satellite-
420 limited regions with heavy snow.

421 Figure 6 presents the Spearman rank correlation depending on the SWE amount in the
422 Northern Hemisphere. AMSR2 exhibits higher performance than Openloop for SWE up to 16
423 mm. However, the performance of AMSR2 sharply declines beyond that threshold, and
424 Openloop shows a better performance. Consistent with the results illustrated in Figs. 4 and 5,
425 DA demonstrates superior performance compared to others. Note that DA performs
426 significantly better in the transition region of less than 16 mm of SWE. Considering that the
427 area below 16 mm of SWE accounts for approximately 53% of the entire area of the Northern
428 Hemisphere(as shown in the pie chart in Fig. 6), the data assimilation impact is identifiable,
429 and it can contribute substantially to the increase in the prediction skill through improving the

430 simulation of the albedo changes and surface energy balance.

431 Consistent with the description in Section 3.3, this study considers an algorithm based on
432 the highly reliable IMS satellite SCF data to identify the presence of snow and determine the
433 assimilation process. Therefore, a further sensitivity test is conducted to investigate the
434 influence of incorporating IMS data in snow assimilation. Figure 7 compares the correlation
435 differences between Openloop and the data assimilation result employing both AMSR2 and
436 IMS (DA), as well as the data assimilation result utilizing solely AMSR2 and excluding IMS
437 (hereafter referred to as DA_AMSR2). The results obtained from the snow assimilation show
438 the improvements in the transitional regions where AMSR2 denotes a better agreement with
439 the observations compared to Openloop. Notably, the skill is enhanced significantly in DA by
440 incorporating the IMS SCF. DA exhibits inferior performance compared to Openloop in certain
441 exceptional cases, which may be attributed to discrepancies in snow identification between the
442 CMC observations used for correlation and the IMS data utilized for data assimilation.
443 Moreover, the performance of SWE improves even when only AMSR2 is used, but
444 incorporating IMS leads to a substantial improvement in the transitional regions. This implies
445 that IMS has a positive influence on the snow data assimilation.

446

447 **4.2 Kalman gain analysis**

448 In order to better understand the skill enhancement through snow assimilation of satellite
449 data, this section examines the Kalman gain. Figure 8 illustrates the spatial distribution of
450 observation error, model background error, and the Kalman gain. A high value of the Kalman
451 gain denotes that the assimilated result is closer to the AMSR2 observation than the model
452 background. The Kalman gain is large when the background error becomes large, or the
453 observation error is small. As this study specifies the observation error as a conservative 10%
454 of SWE compared to the previous study (Lee et al., 2015), the observation error basically

455 follows the distribution similar to the climatological-mean values. The background errors,
456 originating from the 24 ensemble members, have higher values in high-latitude regions and
457 mid-latitude regions. Data assimilation methods such as LETKF used in this study often face
458 challenges in accurately representing background errors when the ensemble spread is
459 insufficient. Generally, the magnitude of ensemble spread is frequently compared to the root
460 mean square error (RMSE). The ensemble spread in this study demonstrates a sufficiently valid
461 magnitude in comparison with the RMSE, as illustrated in SFig. 1, indicating that it is well
462 estimated. Moreover, the SWE distribution among ensemble members consistently exhibited a
463 Gaussian distribution, with a distinct this distribution particularly evident in transitional regions
464 (SFig. 4). In the spatial distribution of Kalman gain in Fig. 8c, significant performance
465 improvement is observed in transition regions, where Kalman gains exhibit larger values.
466 However, in high-latitude areas with substantial snow accumulation, there is a tendency for
467 Kalman gain to have lower values. These findings agree well with the bar graph in Fig. 9, which
468 illustrates the Kalman gain as a function of SWE amount. In the region encompassing the
469 transition region with SWE amounts below 20 mm, the Kalman gain displays the highest values,
470 particularly exceeding 0.8. As the SWE amount increases, the Kalman gain decreases, with a
471 significant decline observed when the SWE amount reaches 80-100 mm or higher. Furthermore,
472 in the areas where DA denotes improved skill compared to Openloop, the Kalman gain shows
473 values generally above 0.7. In contrast, relatively lower values below 0.5 are observed in the
474 areas with decreased skill. This indicates that in the dominant areas of performance
475 improvement, including the transition region, the background error is significantly larger than
476 the observation error, emphasizing the substantial influence of observations in data assimilation.
477 It is found that accurate remote sensing retrievals are well reflected in regions with high
478 uncertainty in the LSM through the snow data assimilation system, leading to performance
479 improvement.

480 **4.3 Validation of the SWE for the extreme event**

481 In April 2020, Siberia experienced a record-breaking heatwave with the highest observed
482 average temperature. This section investigates the potential benefits of snow assimilation using
483 satellite data for the case of the 2020 Siberian heatwave. Previous studies have identified the
484 strong polar vortex accompanied by the AO amplification during winter as a major cause of
485 the cold Eurasian region (Overland and Wang, 2021). Additionally, it has been revealed that
486 the occurrence of high temperatures in the Siberian region is found to be closely associated
487 with large-scale atmospheric waves in the upper atmosphere over the Eurasian region
488 originating from the Atlantic (De Angelis et al., 2023). As a result, remarkable snow melting
489 occurred due to the high surface temperature over the Siberian region in April 2020, leading to
490 extremely low values of SWE and SCF as depicted in SFig. 2. This is consistent with previous
491 studies reporting a significant snow depletion in 2020 in the region (Gloege et al., 2022).
492 Especially, as shown in Fig. 10, significant negative anomalies in SWE and SCF are
493 predominant over the transition region. Substantial snow melt can contribute to record-
494 breaking heatwaves through albedo feedback and changes in the ratio of the latent and sensible
495 heat fluxes from the exposed surface, coupled with favorable atmospheric circulation patterns
496 (Collow et al., 2022). Collow et al. (2022) demonstrated that the exposed surface contributed
497 to up to 20% of the temperature anomaly over Siberia in spring 2020. This implies the
498 importance of realistic snow initial states in the global coupled model forecasts. For the
499 Siberian region with extreme high-temperature events marked by the red box in Fig. 10, DA
500 shows a better agreement with the extremely dry snow conditions, especially in the transitional
501 region, compared to the Openloop. These results are evident when considering the observation-
502 to-model ratio in that region. The percentage of CMC (IMS) is 83% (78%) for Openloop and
503 93% (89%) for DA, indicating that DA with snow data assimilation based on satellite data
504 effectively replicates the observed snow depletion in comparison with Openloop. Similarly to

505 the 2020 case, we obtained another significant case in 2014 compared to Openloop, as shown
506 in SFig. 3. Such extremely dry snow conditions can provide significant heatwave events in the
507 following months.

508

509

510

511

512

513

514 **5. Conclusions and discussion**

515 The advanced SWE data assimilation is developed in this study with the LETKF data
516 assimilation method and the JULES LSM. The system assimilates snow water equivalent
517 retrievals from AMSR2 and IMS snow cover. This constitutes an objective way to optimally
518 combine two imperfect data sources for SWE from satellite remote sensing data and the land
519 surface model simulation forced by observed atmospheric data. This study shows that the
520 satellite-derived SWE has limitations in penetrating deep snow and exhibited much
521 discrepancy from the SWE obtained from the Openloop LSM simulations. The SWE
522 assimilation in this study proves the beneficial impacts of using satellite snow data, maintaining
523 better analysis quality by dynamically balancing the errors from the satellite observations and
524 the model background states.

525 It is found that the simulation from Openloop as a baseline shows superior performance in
526 high-latitude regions with heavy snow accumulation but relatively inferior performance in
527 transition regions with much variation of snow in space and time. Contrastingly, the AMSR2
528 satellite data represent poor performance in high-latitude regions but exhibit relatively better
529 performance in the transition regions. The SWE from the LETKF data assimilation consistently
530 exhibits better performance in capturing the climatology and temporal variation compared to
531 other results. It specifically improves the analysis in the mid-latitude transition regions that
532 cover approximately 53% of the entire areas of the Northern Hemisphere. It is found that the
533 model background errors estimated from the ensemble spread are significantly larger than the
534 observation errors, thereby reflecting satellite information more in those regions. The LETKF
535 data assimilation also proves reliable representation in the heavy snow regions due to low
536 ensemble spread and large uncertainty in the satellite retrievals. Moreover, during the record-
537 breaking heatwave in Siberia in April 2020, the remarkable snow depletion observed due to
538 high surface temperatures is more realistically reproduced by our snow analysis compared to

539 the Openloop.

540 This snow data assimilation framework is anticipated to contribute to a more precise
541 prediction of atmospheric conditions by realistically capturing the interaction between the
542 atmosphere and land, given the substantial influence of SWE on energy and water balance at
543 the interface of the atmosphere and land. Specifically, this applies to the transitional regions
544 with high spatial and temporal variability. The long-term analysis of snow manifests a
545 pronounced variability in the continental interior at the interannual timescales, potentially
546 improving the prediction of extreme heatwave events by global climate models. This study
547 used the gridded CMC data from in-situ observations for the validation. Although existing
548 snow data are subject to much uncertainty and limitations, we expect to obtain comparable
549 conclusions and significant benefits of optimally combining satellite SWE data and the LSM
550 model simulations through LETKF data assimilation method.

551 The quality of the observation is crucial in the data assimilation system. Satellite-derived
552 snow cover exhibits a significantly higher accuracy compared to other data sources, while SWE
553 has restricted performance due to the limitations of penetration depth by satellite sensors and
554 relies heavily on estimation algorithms. Due to these problems, most previous studies and
555 operational centers primarily depend on satellite-derived snow cover for snow initialization.
556 However, the findings from this study highlighted the beneficial impacts of using satellite-
557 derived SWE, particularly in the rapidly changing transition areas, to find out which variable
558 is more important in closing surface energy and water balance changed by snow. Nevertheless,
559 areas of significance in large-scale circulation, such as the Tibetan region, which experiences
560 significant uncertainty and degraded performance in satellite data, do not exhibit substantial
561 data assimilation effects. As the performance of SWE derived from various satellites continues
562 to advance, these issues will be discussed more.

563

564 **Key words**

565 Snow data assimilation, AMSR2, LETKF, snow water equivalent, JULES LSM

566

567 ***Data availability.***

568 The AMSR2 SWE and IMS SC were obtained from
569 https://n5eil01u.ecs.nsidc.org/AMSA/AU_DySno.001/ and
570 <https://noaadata.apps.nsidc.org/NOAA/G02156/>, respectively. The CMC SWE was collected
571 from https://daacdata.apps.nsidc.org/pub/DATASETS/nsidc0447_CMC_snow_depth_v01/.

572 The snow-assimilated results and land surface variables from the LSM offline simulation may
573 be requested from the authors.

574

575 ***Author contributions.***

576 LJI conceived the project, designed the study, developed the snow assimilation system, wrote
577 the paper, and made the figures. LMI provided advice on the methods, project design, and
578 review and editing of the manuscript. TSL helped with the experiment with the land surface
579 model. SEK helped with the data assimilation method based on LETKF. LYK provided advice
580 on snow satellite data and the sensitivity methods. All authors contributed to the writing of the
581 paper by providing comments and feedback.

582

583 ***Competing interests.***

584 The contact author has declared that none of the authors has any competing interests.

585

586 ***Acknowledgements***

587 This work was funded by the Korea Meteorological Administration Research and Development
588 Program under Grant KMI2021-01210. ES was supported by Learning & Academic research
589 institution for Master's·PhD students, and Postdocs (LAMP) Program of the National Research
590 Foundation of Korea (NRF) grant funded by the Ministry of Education (RS-2023-000301702).

591

592

593

594 **Reference**

595 Allen, R.J., Zender, C.S.: Forcing of the Arctic Oscillation by Eurasian snow cover. *J. Clim.* 24 (24),
596 6528-6539, 2011.

597 Best, M.J., Pryor, M., Clark, D.B., Rooney, G.G., Essery, R., Ménard, C.B., Edwards, J.M., Hendry, M.A.,
598 Porson, A., Gedney, N., Mercado, L.M., Sitch, S., Blyth, E., Boucher, O., Cox, P.M.,
599 Grimmond, C.S.B., Harding, R.J.: The Joint UK Land Environment Simulator (JULES), model
600 description–Part 1: energy and water fluxes. *Geosci. Model Dev.* 4, 677–699, 2011.

601 Boone, A., Habets, F., Noilhan, J., Clark, D., Dirmeyer, P., Fox, S., Gusev, Y., Haddeland, I., Koster, R.,
602 Lohmann, D., Mahanama, S., Mitchell, K., Nasonova, O., Niu, G.Y., Pitman, A., Polcher, J.,
603 Shmakin, A., Tanaka, K., van den Hurk, B., Verant, S., Verseghy, D., Viterbo, P., Yang, Z.L.: The
604 Rhone-Aggregation land surface scheme intercomparison project: an overview. *J. Clim.* 17,
605 187–208, 2004.

606 Brasnett, B.: A global analysis of snow depth for numerical weather prediction. *J. Appl. Meteorol.* 38
607 (6), 726–740, 1999.

608 Brown, L.C., Howell, S.E., Mortin, J., Derksen, C.: Evaluation of the Interactive Multisensor Snow and
609 Ice Mapping System (IMS) for monitoring sea ice phenology. *Remote Sens. Environ.* 147,
610 65–78. doi: 10.1016/j.rse.2014.02.012, 2014.

611 Brown, R.D., Brasnett, B.: Canadian Meteorological Centre (CMC) Daily Snow Depth Analysis Data.
612 NASA National Snow and Ice Data Center Distributed Active Archive Center, Boulder,
613 Colorado, USA. <https://doi.org/10.5067/W9FOYWH0EQZ3>, 2010.

614 Brown, R.D., Brasnett, B., Robinson, D.: Gridded North American monthly snow depth and snow
615 water equivalent for GCM evaluation. *Atmos.–Ocean*, 41, 1–14, 2003.

616 Broxton, P.D., Zeng, X., Dawson, N.: The impact of a low bias in snow water equivalent initialization
617 on CFS seasonal forecasts. *J. Clim.* 30 (21), 8657–8671. [https://doi.org/10.1175/JCLI-D-17-](https://doi.org/10.1175/JCLI-D-17-0072.1)
618 0072.1, 2017.

619 Brubaker, K., Pinker, R., Deviatova, E.: Evaluation and comparison of MODIS and IMS snow-cover
620 estimates for the continental United States using station data. *J. Hydrometeorol.* 6, 1002–
621 1017, 2009.

622 Burke, E. J., Dankers, R., Jones, C. D., and Wiltshire, A. J.: A retrospective analysis of pan Arctic
623 permafrost using the JULES land surface model, *Clim. Dynam.*, 41, 1025–
624 1038, <https://doi.org/10.1007/s00382-012-1648-x>, 2013.

625 Chen, M., Wang, W., Kumar, A.: Prediction of monthly-mean temperature: The roles of atmospheric
626 and land initial conditions and sea surface temperature *J. Clim.* 23(3), 717-725, 2010.

627 Cho, E., Tuttle, S.E., Jacobs, J.M.: Evaluating consistency of snow water equivalent retrievals from
628 passive microwave sensors over the north central US: SSM/I vs. SSMIS and AMSR-E vs.
629 AMSR2. *Remote Sens.* 9(5), 465, 2017.

630 Cohen, J., Barlow, M., Kushner, P. J., Saito, K.: Stratosphere–troposphere coupling and links with
631 eurasian land surface variability. *J. Clim.* 20(21), 5335–5343.
632 <https://doi.org/10.1175/2007jcli1725.1>, 2007.

633 Collow, A.B.M., Thomas, N.P., Bosilovich, M.G., Lim, Y.K., Schubert, S.D., Koster, R.D.: Seasonal variability
634 in the mechanisms behind the 2020 Siberian heatwaves. *J. Clim.* 35(10), 3075–3090, 2022.

635 Dawson, N., Broxton, P., Zeng, X.: Evaluation of remotely sensed snow water equivalent and snow
636 cover extent over the contiguous United States. *J. Hydrometeorol.* 19 (11), 1777–1791.
637 <https://doi.org/10.1175/JHM-D-18-0007.1>, 2018.

638 De Angelis, A.M., Schubert, S.D., Chang, Y., Lim, Y.K., Koster, R.D., Wang, H., Marquardt Collow, A.B.:
639 Dynamical Drivers of the Exceptional Warmth over Siberia during the Spring of 2020. *J.*
640 *Clim.* 36(15), 4837–4861, 2023.

641 De Lannoy, G.J.M., Reichle, R.H., Houser, P.R., Arsenault, K.R., Verhoest, N.E.C., Pauwels, V.R.N.: Satellite-
642 scale snow water equivalent assimilation into a high-resolution land surface model. *J.*
643 *Hydrometeorol.* 11 (2), 352–369. <https://doi.org/10.1175/2009JHM1192.1>, 2010.

644 De Rosnay, P., Balsamo, G., Albergel, C., Muñoz-Sabater, J., Isaksen, L. Initialisation of land surface
645 variables for numerical weather prediction. *Surv. Geophys.* 35, 607–621, 2014.

646 Dee, D., Uppala, S., Simmons, A., Berrisford, P., Poli, P., Kobayashi, S., Andrae, U., Balsameda, M.,
647 Balsamo, G., Bauer, P., Bechtold, P., Beljaars, A.C.M., van de Berg, L., Bidlot, J., Bormann, N.,
648 Delsol, C., Dragani, R., Fuentes, M., Geer, A.J., Haimberger, L., Healy, S.B., Hersbach, H., Hólm,
649 E.V., Isaksen, L., Kållberg, P., Köhler, M., Matricardi, M., McNally, A.P., Monge-Sanz, B.M.,
650 Morcrette, J.-J., Park, B.-K., Peubey, C., de Rosnay, P., Tavolato, C., Thépaut, J.-N., Vitart, F.: The
651 ERA-Interim reanalysis: Configuration and performance of the data assimilation system. *Q.*
652 *J. R. Meteorol. Soc.* 137, 553–597, 2011.

653 Derome J, Lin H, Brunet, G.: Seasonal forecasting with a simple general circulation model: Predictive
654 skill in the AO and PNA. *J. Clim.*, 15, 597–609, 2005.

655 Dirmeyer, P.A.: The terrestrial segment of soil moisture–climate coupling. *Geophys. Res. Lett.* 38(16),
656 2011.

657 Dirmeyer, P.A., Gao, X., Zhao, M., Guo, Z., Oki, T., Hanasaki, N.: The Second Global Soil Wetness
658 Project (GSWP-2): Multi-model analysis and implications for our perception of the land
659 surface. *Bull. Amer. Meteor. Soc.* 87, 1381–1397, 2006.

660 Dutra, E., Schär, C., Viterbo, P., Miranda, P. M.: Land-atmosphere coupling associated with snow
661 cover. *Geophys. Res. Lett.* 38 (15) , 2011.

662 Dziubanski, D.J., Franz, K.J.: Assimilation of AMSR-E snow water equivalent data in a spatially-lumped
663 snow model. *J. Hydrol.* 540, 26–39. <https://doi.org/10.1016/j.jhydrol.2016.05.046>, 2016.

664 Essery, R.L.H., Rutter, N., Pomeroy, J., Baxter, R., Stahli, M., Gustafsson, D., Barr, A., Bartlett, P., Elder,
665 K.: SNOWMIP2: an evaluation of forest snow process simulations. *Bull. Amer. Meteor. Soc.*
666 90, 1120–1135, 2009.

667 Eagleson, P.S.: *Dynamic Hydrology*, McGraw-Hill, 1970

668 Foster, J.L., Sun, C., Walker, J.P., Kelly, R., Chang, A., Dong, J., Powell, H.: Quantifying the uncertainty
669 in passive microwave snow water equivalent observations. *Remote Sens. Environ.* 94, 187–
670 203, 2005.

671 Gan, Y., Zhang, Y., Kongoli, C., Grassotti, C., Liu, Y., Lee, Y. K., Seo, D. J.: Evaluation and blending of

672 ATMS and AMSR2 snow water equivalent retrievals over the conterminous United
673 States. *Remote Sens. Environ.* 254, 112280, 2021.

674 Gloege, L., Kornhuber, K., Skulovich, O., Pal, I., Zhou, S., Ciais, P., Gentine, P.: Land-Atmosphere Cascade
675 Fueled the 2020 Siberian Heatwave. *AGU Advances*, 3 (6), e2021AV000619, 2022.

676 Hamill, T.M., Whitaker, J.S., Snyder, C.: Distance-dependent filtering of background error covariance
677 estimates in an ensemble Kalman filter. *Mon. Weather Rev.* 129, 2776–2790, 2001.

678 Helfrich, S.R., McNamara, D., Ramsay, B.H., Baldwin, T., Kasheta, T.: Enhancements to, and forthcoming
679 developments in the interactive multisensor snow and ice mapping system (IMS). *Hydrol.*
680 *Process.* 21 (12), 1576–1586. <https://doi.org/10.1002/hyp.6720>, 2007.

681 Helmert, J., Şensoy Şorman, A., Montero, R.A., De Michele, C., De Rosnay, P., Dumont, M., Finger, D.,
682 Lange, M., Picard, G., Potopová, V., et al.: Review of Snow Data Assimilation Methods for
683 Hydrological, Land Surface, Meteorological and Climate Models: Results from a COST
684 HarmoSnow Survey. *Geoscience*, 8 (12), 489, 2018.

685 Houtekamer, P.L., Mitchell, H.L.: A sequential ensemble Kalman filter for atmospheric data
686 assimilation. *Mon. Weather Rev.* 129, 123–137, 2001.

687 Huning, L.S., AghaKouchak, A.: Global snow drought hot spots and characteristics. *Proc. Natl. Acad.*
688 *Sci.* 117(33), 19753–19759, 2020.

689 Hunt, B.R., Kostelich, E.J., Szunyogh, I.: Efficient data assimilation for spatiotemporal chaos: a local
690 ensemble transform Kalman filter. *Phys. D Nonlinear Phenom.* 230, 112–126, 2007.

691 Imaoka, K., Kachi, M., Kasahara, M., Ito, N., Nakagawa, K., Oki, T.: Instrument performance and
692 calibration of AMSR-E and AMSR2. *Int. Arch. Photogramm. Remote. Sens. Spat. Inf. Sci.* 38
693 (8), 13–16, 2010.

694 Jeong, J.H., Linderholm, H.W., Woo, S.H., Folland, C., Kim, B.M., Kim, S.J., Chen, D.: Impacts of snow
695 initialization on subseasonal forecasts of surface air temperature for the cold season. *J.*
696 *Clim.* 26 (6), 1956–1972, 2013.

697 Kobayashi, S., Ota, Y., Harada, Y., Ebata, A., Moriya, M., Onoda, H., Onogi, K., Kamahori, H., Kobayashi,
698 C., Endo, H.: The JRA-55 reanalysis: general specifications and basic characteristics. *J.*
699 *Meteorol. Soc. Jpn. Ser. II* 93, 5–48, 2015.

700 Koster, R.D., Dirmeyer, P.A., Guo, Z., Bonan, G., Chan, E., Cox, P., Gordon, C.T., Kanae, S., Kowalczyk,
701 E., Lawrence, D., Liu, P., Lu, C.H., Malyshev, S., McAvaney, B., Mitchell, K., Mocko, D., Oki,
702 T., Oleson, K., Pitman, A., Sud, Y.C., Taylor, C.M., Verseghy, D., Vasic, R., Xue, Y., Yamada,
703 T., GLACE Team: Regions of strong coupling between soil moisture and
704 precipitation. *Science*, 305 (5687), 1138–
705 1140, <https://doi.org/10.1126/science.1100217>, 2004.

706 Koster, R.D., Mahanama, S., Yamada, T., Balsamo, G., Berg, A., Boisserie, M., Dirmeyer, P., Doblas-Reyes,
707 F., Drewitt, G., Gordon, C.: The second phase of the global land–atmosphere coupling
708 experiment: soil moisture contributions to subseasonal forecast skill. *J. Hydrometeorol.* 12,
709 805–822, 2011.

710 Kumar, S.V., Jasinski, M., Mocko, D.M., Rodell, M., Borak, J., Li, B., Beaudoin, H.K., Peters-Lidard, C.D.:

711 NCA-LDAS land analysis: development and performance of a multisensor, multivariate land
712 data assimilation system for the national climate assessment. *J. Hydrometeorol.* 20 (8), 1571–
713 1593. <https://doi.org/10.1175/JHM-D-17-0125.1>, 2019.

714 Kwon, Y., Yang, Z.-L., Hoar, T.J., Toure, A.M.: Improving the radiance assimilation performance in
715 estimating snow water storage across snow and land-cover types in North America. *J.*
716 *Hydrometeorol.* 18 (3), 651–668. <https://doi.org/10.1175/JHM-D-16-0102.1>, 2017.

717 Li, F., Orsolini, Y.J., Keenlyside, N., Shen, M.L., Counillon, F., Wang, Y.G.: Impact of snow initialization
718 in subseasonal-to-seasonal winter forecasts with the Norwegian Climate Prediction
719 Model. *J. Geophys. Res. Atmos.* 124 (17-18), 10033-10048, 2019.

720 Li, F., Wang, H.: Autumn Eurasian snow depth, autumn Arctic sea ice cover and East Asian winter
721 monsoon. *Int. J. Climatol.* 34(13), 3616-3625, 2014.

722 Lim, S., Gim, H.J., Lee, E., Lee, S., Lee, W.Y., Lee, Y.H., Cassardo C., Park, S.K.: Optimization of snow-
723 related parameters in the Noah land surface model (v3. 4.1) using a micro-genetic algorithm
724 (v1. 7a). *Geosci. Model Dev.* 15(22), 8541-8559, 2022.

725 Liu, Y., Peters-Lidard, C.D., Kumar, S.V., Arsenault, K.R., Mocko, D.M.: Blending satellite-based snow
726 depth products with in situ observations for streamflow predictions in the upper Colorado
727 River basin. *Water Resour. Res.* 51 (2), 1182–1202. <https://doi.org/10.1002/2014WR016606>,
728 2015.

729 Lee, Y.K., Kongoli, C., Key, J.: An in-depth evaluation of heritage algorithms for snow cover and snow
730 depth using AMSR-E and AMSR2 measurements. *J. Atmos. Ocean. Technol.* 32(12), 2319-
731 2336, 2015.

732 Meng, J., Yang, R., Wei, H., Ek, M., Gayno, G., Xie, P., Mitchell, K.: The land surface analysis in the
733 NCEP climate forecast system reanalysis. *J. Hydrometeorol.* doi:10.1175/JHM-D-11-090.1,
734 2012.

735 Meyal, A.Y., Versteeg, R., Alper, E., Johnson, D., Rodzianko, A., Franklin, M., Wainwright, H.: Automated
736 cloud based long short-term memory neural network based SWE prediction. *Front. Water*, 2,
737 574917, 2020.

738 Miyoshi, T., Yamane, S.: Local ensemble transform Kalman filtering with an AGCM at a T159/L48
739 resolution. *Mon. Weather Rev.* 135, 3841–3861, 2007.

740 Orsolini, Y.J., Senan, R., Balsamo, G., Doblas-Reyes, F.J., Vitart, F., Weisheimer, A., Carrasco, A., Benestad,
741 R.E.: Impact of snow initialization on sub-seasonal forecasts. *Clim. Dyn.* 41, 1969-1982, 2013.

742 Orsolini, Y.J., Senan, R., Vitart, F., Weisheimer, A., Balsamo, G., Doblas-Reyes, F.: Influence of the
743 Eurasian snow on the negative North Atlantic Oscillation in subseasonal forecasts of the
744 cold winter 2009/10. *Clim. Dyn.* 47(3-4), 1325–1334. <https://doi.org/10.1007/s00382-015-2903-8>, 2016.

745

746 Overland, J. E., Wang, M.: The 2020 Siberian heat wave. *Int. J. Climatol.* 41, E2341-E2346, 2021.

747 Pullen, S., Jones, C., Rooney, G.: Using satellite-derived snow cover data to implement a snow analysis
748 in the met office NWP model. *J. Appl. Meteorol.* 50, 958–973. doi:10.1175/2010JAMC2527.1,
749 2011.

750 Pulliainen, J., Luojus, K., Derksen, C., Mudryk, L., Lemmetyinen, J., Salminen, M., Ikonen, J., Takala, M.,
751 Cohen, J., Smolander, T., Norberg, J.: Patterns and trends of Northern Hemisphere snow mass
752 from 1980 to 2018. *Nature*, 581 (7808), 294–298. [https://doi.org/10.1038/s41586-020-2258-](https://doi.org/10.1038/s41586-020-2258-0)
753 0, 2020.

754 Ramsay, B.H.: The interactive multisensor snow and ice mapping system. *Hydrol. Process.* 12 (10-11),
755 1537–1546, 1998.

756 Reichle, R.H.: Data assimilation methods in the Earth sciences. *Adv. Water Resour.* 31, 1411–1418,
757 2008.

758 Reichle, R.H., Draper, C.S., Liu, Q., Girotto, M., Mahanama, S.P., Koster, R.D., De Lannoy, G.J.:
759 Assessment of MERRA-2 land surface hydrology estimates. *J. Clim.* 30 (8), 2937-2960, 2017.

760 Reichle, R.H., Koster, R.D.: Bias reduction in short records of satellite soil moisture. *Geophys. Res. Lett.*
761 31, 2004.

762 Reichle, R.H., Koster, D., De Lannoy, G.J.M., Forman, B.A., Liu, Q., Mahanama, S.P.P., Toure, A.M.:
763 Assessment and Enhancement of MERRA Land Surface Hydrology Estimates. *J. Clim.* 24,
764 6322–6338, 2011.

765 Seo, E., Lee, M.I., Jeong, J.H., Koster, R.D., Schubert, S.D., Kim, H.M., Kim, D.H., Kang H.S., Kim, H.K.,
766 MacLachlan, C., Scaife, A.A.: Impact of soil moisture initialization on boreal summer
767 subseasonal forecasts: mid-latitude surface air temperature and heat wave
768 events. *Clim. Dyn.* 52, 1695-1709, 2019.

769 Seo, E., Lee, M.I., Reichle, R.H.: Assimilation of SMAP and ASCAT soil moisture retrievals into the
770 JULES land surface model using the Local Ensemble Transform Kalman Filter. *Remote Sens.*
771 *Environ.* 253, 112222, 2021.

772 Seo, E., Lee, M.I., Schubert, S.D., Koster, R.D., Kang, H.S.: Investigation of the 2016 Eurasia heat wave
773 as an event of the recent warming. *Environ. Res. Lett.* 15(11), 114018, 2020.

774 Shlyayeva, A., Tolstykh, M., Mizyak, V., Rogutov, V.: Local ensemble transform Kalman filter data
775 assimilation system for the global semi-Lagrangian atmospheric model. *Russ. J. Numer. Anal.*
776 *Math. Model.* 28(4), 419-442, 2013.

777 Sturm, M., Taras, B., Liston, G.E., Derksen, C., Jonas, T., Lea, J.: Estimating snow water equivalent using
778 snow depth data and climate classes. *J. Hydrometeor.* 11, 1380–1394, 2010.

779 Su, H., Yang, Z.-L., Dickinson, R.E., Wilson, C.R., Niu, G.-Y.: Multisensor snow data assimilation at the
780 continental scale: The value of gravity recovery and climate experiment terrestrial water
781 storage information. *J. Geophys. Res.*, 115, D10104, doi:10.1029/2009JD013035, 2010.

782 Takala, M., Luojus, K., Pulliainen, J., Derksen, C., Lemmetyinen, J., Karna, J.P., Koskinen, J., Bojkov, B.:
783 Estimating northern hemisphere snow water equivalent for climate research through
784 assimilation of space-borne radiometer data and ground-based measurements. *Remote*
785 *Sens. Environ.* 115:3517–3529, 2011.

786 Thomas, J.A., Berg, A.A., Merryfield, W.J.: Influence of snow and soil moisture initialization on sub-
787 seasonal predictability and forecast skill in boreal spring. *Clim. Dyn.* 47 (1), 49-65, 2016.

788 Toure, A.M., Luojus, K., Rodell, M., Beaudoin, H., Getirana, A.: Evaluation of simulated snow and

789 snowmelt timing in the Community Land Model using satellite-based products and
790 streamflow observations. *J. Adv. Model. Earth Syst.* 10(11), 2933-2951, 2018.

791 U.S. National Ice Center: IMS daily Northern Hemisphere snow and ice analysis at 1 km, 4 km, and
792 24 km resolutions, version 3. Boulder, Colorado, USA. NSIDC: National Snow and Ice Data
793 Center, accessed: 18 Aug 2022, <https://doi.org/10.7265/N52R3PMC>, 2008.

794 You, Y., Huang, C., Gu, J., Li, H., Hao, X., Hou, J.: Assessing snow simulation performance of typical
795 combination schemes within Noah-MP in northern Xinjiang, China. *J. Hydrol.* 581, 124380,
796 2020.

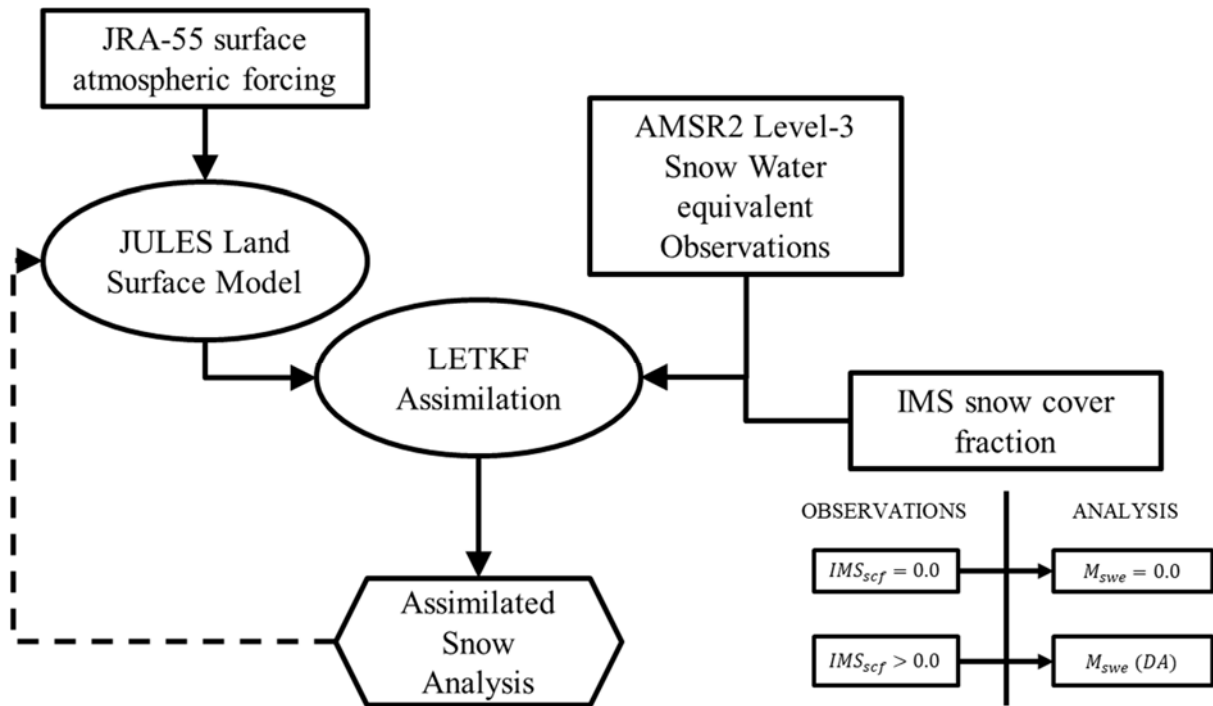
797

798 **Table 1.** Description of the land surface model, the data used, and assimilation experiment
 799 designs.

| | INFORMATION | REFERENCES |
|------------------------------|--|---|
| Land Surface Model | JULES | Best et al., (2011) |
| Atmospheric Forcing | 3-hourly JRA-55 reanalysis | Kobayashi et al., (2015) |
| Snow Observation | AMSR2 & IMS | Imaoka et al., (2010) Ramsay (1998) Helfrich et al., (2007) |
| Data Assimilation scheme | Local Ensemble Transform Kalman Filter (LETKF) | Hunt et al., (2007) Miyoshi and Yamane, (2007) |
| Resolution (km) | 0.5° × 0.5° (~ 50) | |
| | 1-day DA cycle | |
| Localization patch size (km) | 3×3 (150), $\sigma = 30$ | |
| Ensemble sizes | 24 | |
| Experiment period | 2013-2020, APR | |

800

801



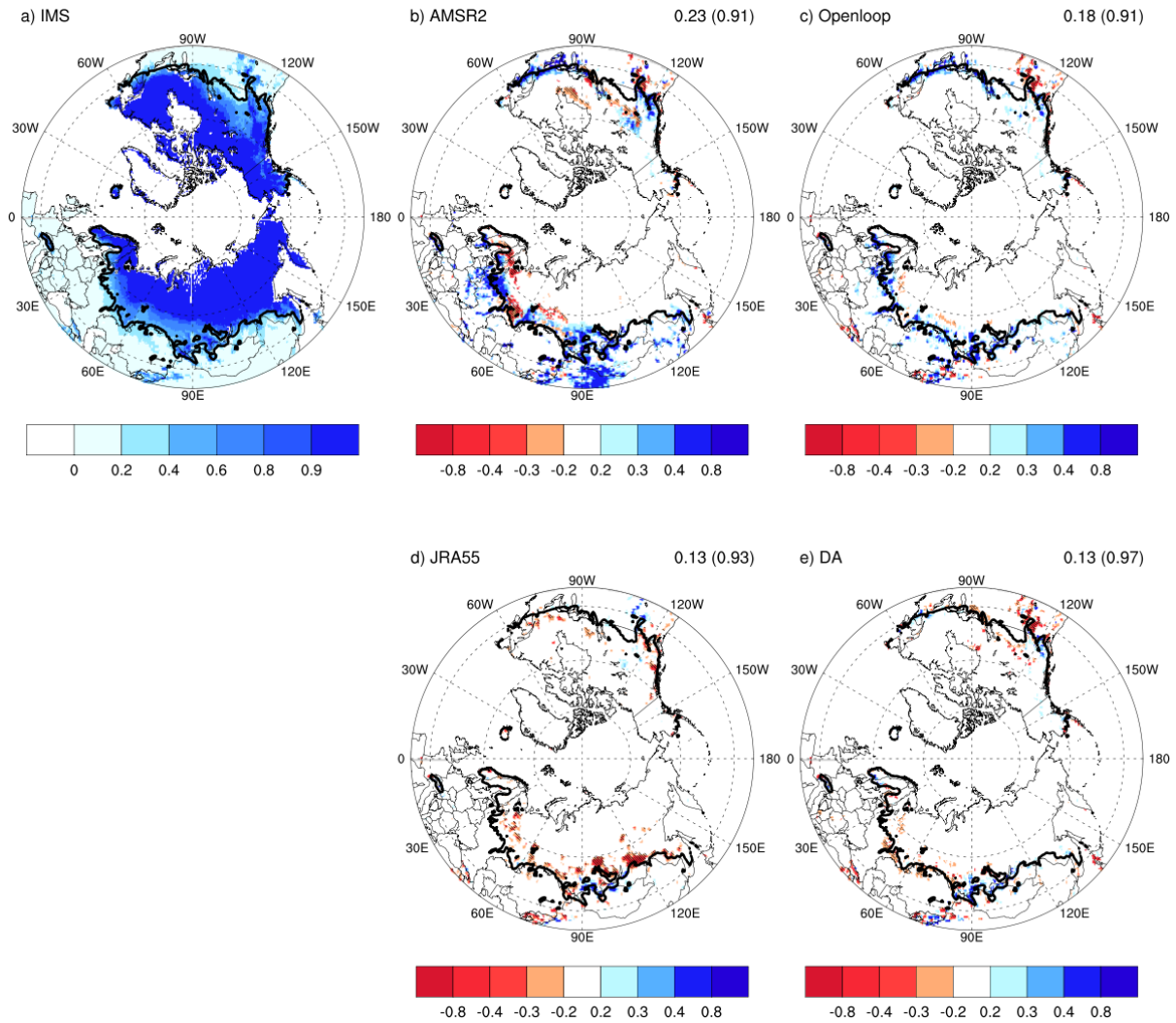
802

803 **Figure 1.** Schematic diagram of the snow assimilation system with satellite-derived

804 observations and the land surface model outputs.

805

806

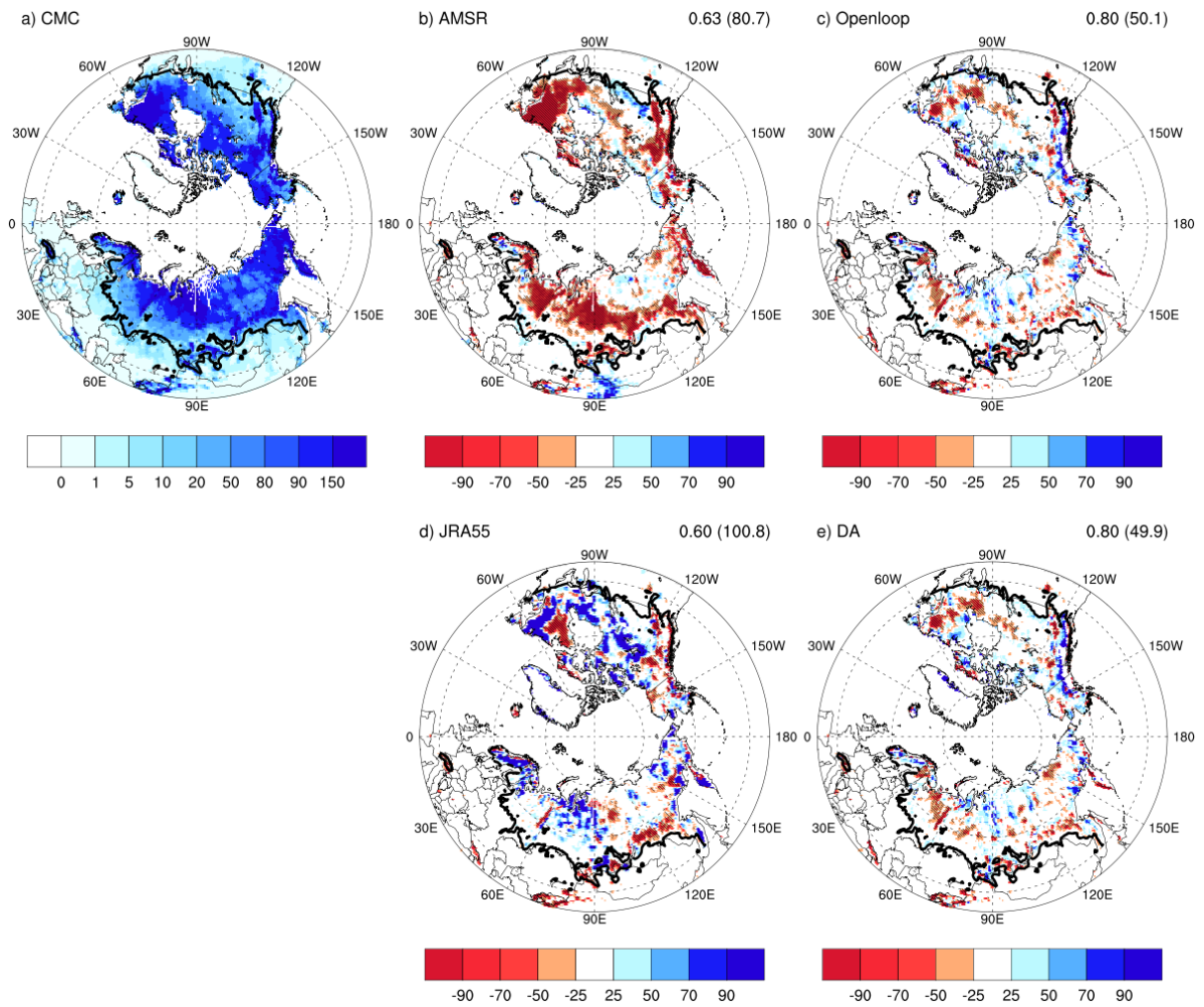


807

808 **Figure 2.** (a) Climatology of SCF from IMS used as reference and (b-e) the differences from
 809 IMS for AMSR2, base-line model simulation (Openloop), JRA55, and the data
 810 assimilation results (DA) for April during 2013-2020. The black line represents the
 811 boundary of the transition region, defined as the climatological-mean SWE of less than
 812 16mm. Each value on the top right is the root-mean-squared difference with IMS and
 813 the accuracy from IMS (parenthesis) for 15323 pixels over 40-60°N. The accuracy is
 814 defined in supplementary Table 1 as in previous study (Lee et al., 2015). Negative
 815 values in red shades are indicated with a diagonal line.

816

817

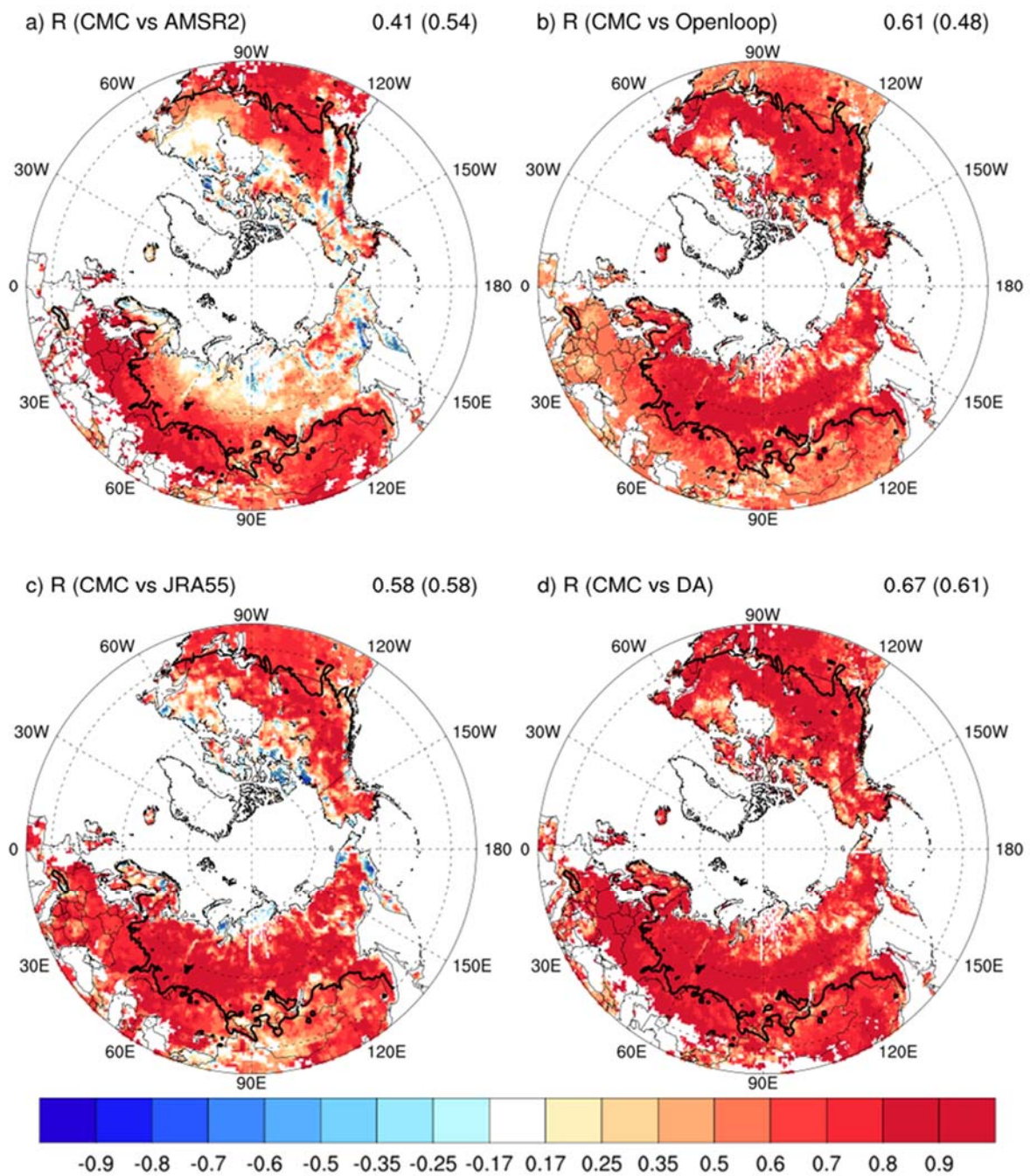


818

819 **Figure 3.** (a) Climatology of SWE from CMC used as reference and (b-e) the differences from
 820 CMC for AMSR2, base-line model simulation (Openloop), JRA55, and the data
 821 assimilation results (DA) for April during 2013-2020. The black line represents the
 822 boundary of the transition region, defined as the climatological-mean SWE of less than
 823 16mm. Each value on the top right is the pattern correlation with CMC for 26482 pixels
 824 over 40 °N and the root-mean-squared difference (unit: kg/m²) from CMC (parenthesis)
 825 for 15323 pixels over 40-60°N. Negative values in red shades are indicated with a
 826 diagonal line.

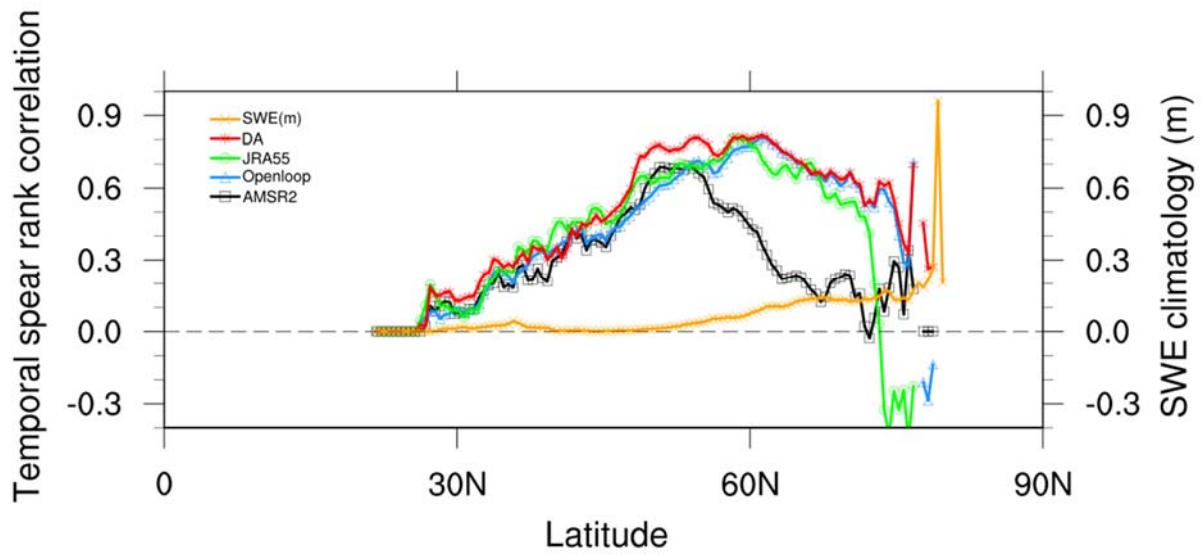
827

828



829

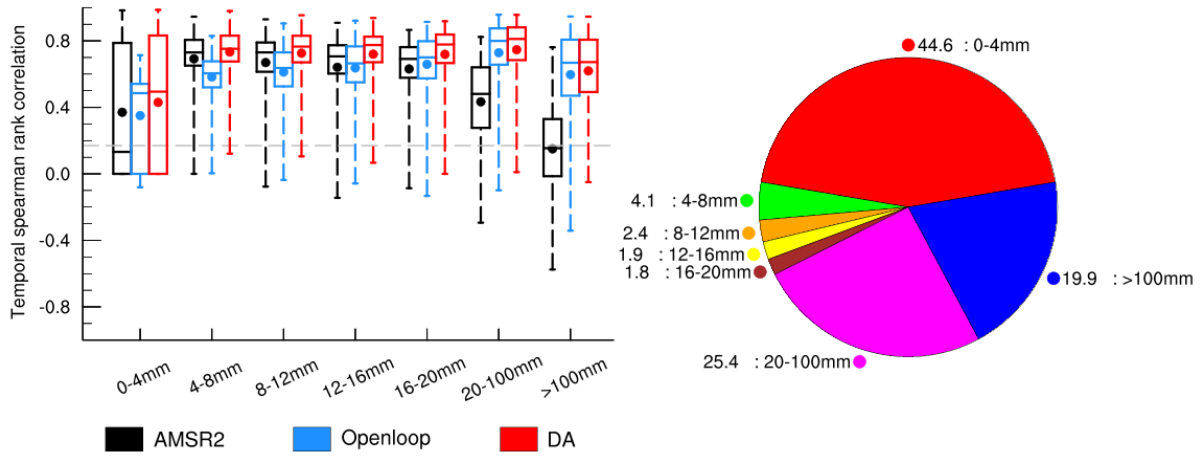
830 **Figure 4.** SWE skill measured as the Spearman rank correlation (R) with the CMC for AMSR2,
 831 base-line model simulation (Openloop), JRA55, and the data assimilation result (DA).
 832 The black line represents the boundary of the transition region, defined as the
 833 climatological-mean SWE of less than 16mm. Each value on the top is the area-average
 834 R of North hemisphere for 26482 pixels over 40°N and for 8801 pixels over the
 835 transition region (parenthesis). Negative values are indicated with a diagonal line.



836

837 **Figure 5.** Zonally-averaged Spearman rank correlation (R) along the latitude for SWE. The
 838 yellow line indicates the climatology of SWE, and the black, blue, green, and red lines
 839 denote the values of AMSR2, base-line model simulation (Openloop), JRA55, data
 840 assimilation results (DA), respectively.

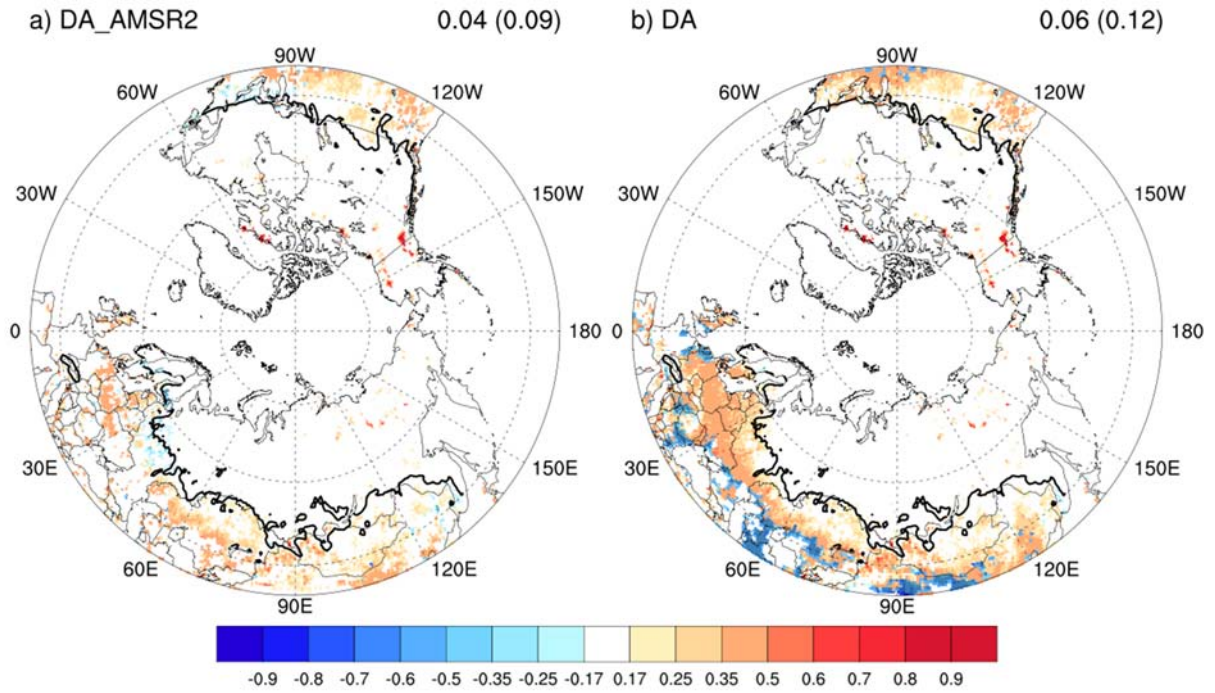
841



842

843 **Figure 6.** Box plots of the Spearman rank correlation (R) according to SWE. The pie chart
 844 shows the total area ratio (%) as a function of SWE amount. The black, blue, and red
 845 boxes denote the AMSR2, base-line model simulation (Openloop), and the data
 846 assimilation results (DA), respectively. The boxes indicate 25 and 75% percentiles, and
 847 the line and point in the boxes shows the median and the mean values. The upper and
 848 lower whiskers denote the 10 and 90% percentiles, respectively.

849



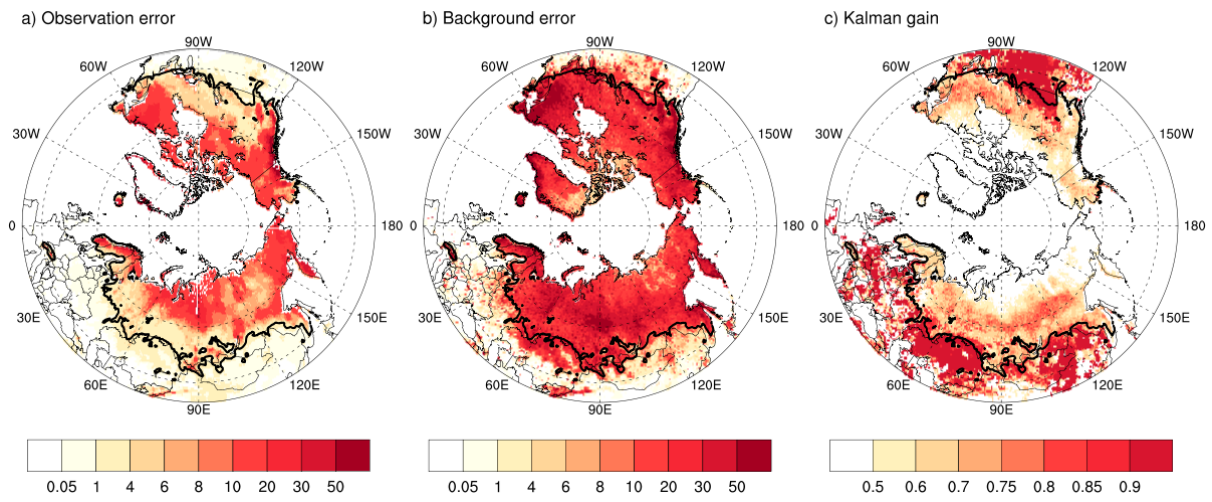
850

851 **Figure 7.** The difference in SWE Spearman rank correlation coefficient with CMC between
 852 the Openloop and data assimilation results: DA employing both AMSR2 and IMS and
 853 DA_AMSR2 utilizing solely AMSR2 and excluding IMS, for April during 2013-2020.
 854 The black line represents the boundary of the transition region, defined as the
 855 climatological-mean SWE of less than 16mm. Each value on the top right is the area-
 856 average over 40°N and the transition region (parenthesis). Negative values are indicated
 857 with a diagonal line.

858

859

860



861

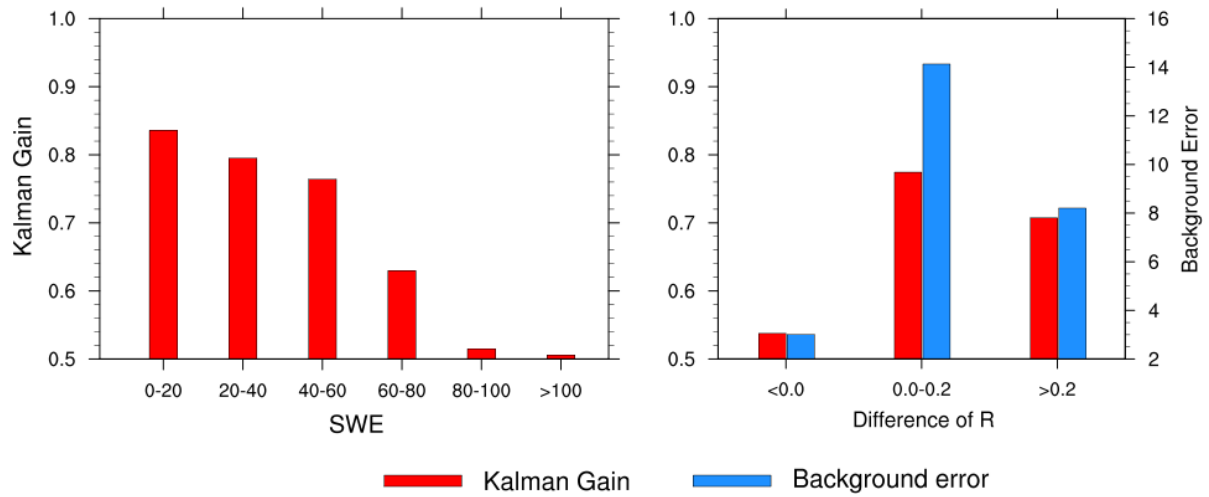
862

863

864

865

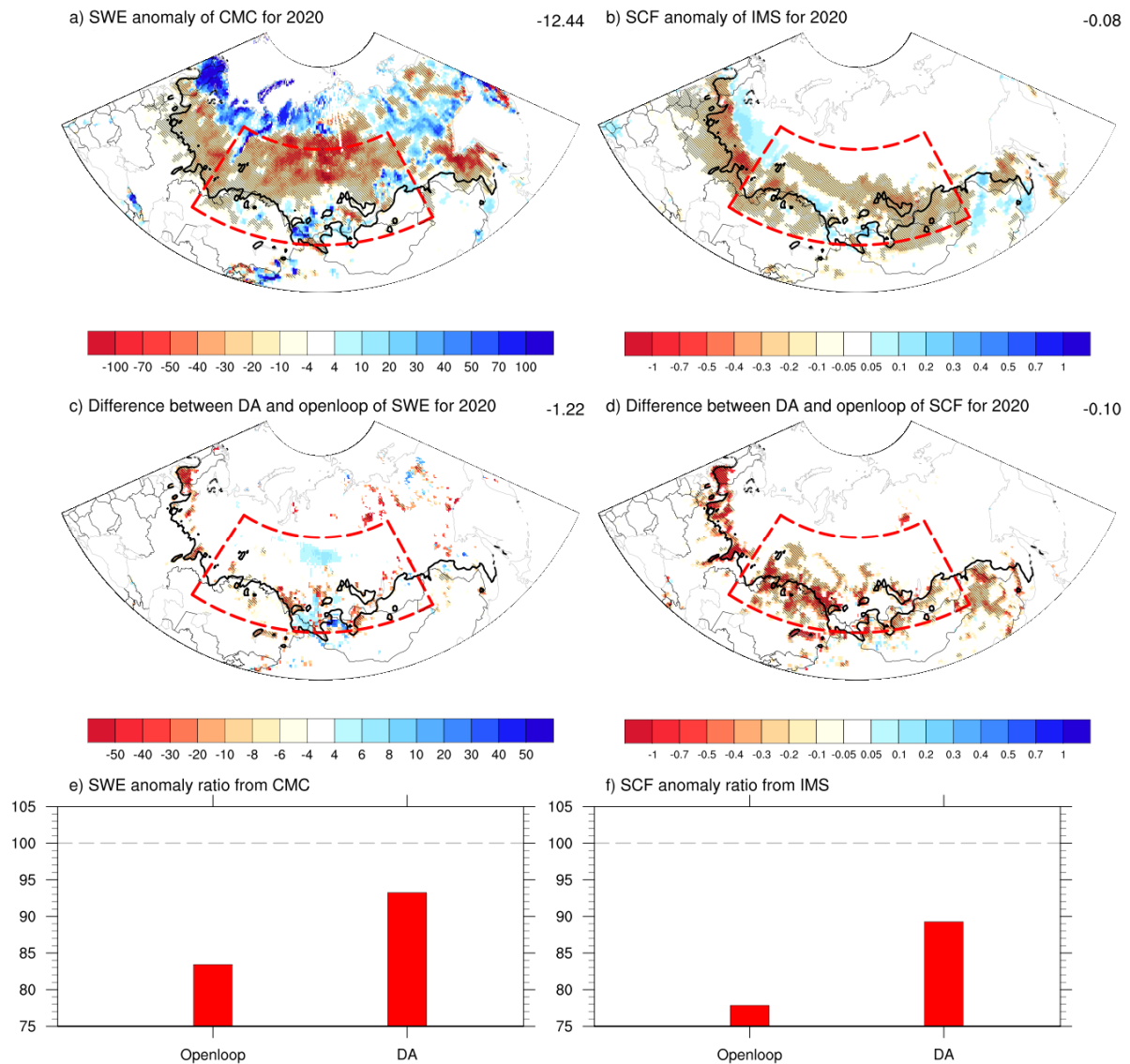
Figure 8. Spatial distribution of observation error (unit: kg/m^2), background error (unit: kg/m^2), and Kalman gain. The black line represents the boundary of the transition region, defined as the climatological-mean SWE of less than 16mm.



866

867 **Figure 9.** Bar chart of (left) the Kalman gain according to the SWE amount, and (right) the
 868 Kalman gain (red line) and background error (blue line) as a function of the difference
 869 between Openloop and DA in Spearman rank correlation coefficient (R).

870



871

872 **Figure 10.** Anomalies of a) SWE from CMC and b) SCF from IMS as well as the difference
 873 (c, d) of variables between DA and openloop in April 2020. Bar chart (e, f) indicates
 874 the ratio of DA and openloop to verification data such as CMC and IMS in the red box
 875 (48–65°N and 55–120°E), which is the region associated with extreme high-
 876 temperature events, focused on this study. Negative values are indicated with a diagonal
 877 line.

878

879